Journal of Food Composition and Analysis 125 (2024) 105857

Contents lists available at ScienceDirect

Journal of Food Composition and Analysis

journal homepage: www.elsevier.com/locate/jfca

# A novel molecularly imprinted electrochemical sensor based on graphitic carbon nitride nanosheets decorated bovine serum albumin@$MnO_2$ nanocomposite for zearalenone detection

Nesrin Çapar Rehman [a], Neslihan Özdemir [b], Havva Boyacıoğlu [c], Mehmet Lütfi Yola [a,*]

[a] Hasan Kalyoncu University, Faculty of Health Sciences, Department of Nutrition and Dietetics, Gaziantep, Turkey
[b] Amasya University, Merzifon Vocational School, Department of Machinery and Metal Technologies, Amasya 05300, Turkey
[c] Pamukkale University, Faculty of Engineering, Department of Chemical Engineering, Denizli, Turkey

ARTICLE INFO

*Keywords:*
Zearalenone
Molecularly imprinting
Graphitic carbon nitride
Rice analysis

ABSTRACT

Zearalenone (ZEA), as a carcinogenic mycotoxin, is widely found in a wide variety of food products such as grains and its carcinogenicity, neurotoxicity, and estrogenic effects on humans were reported. In this report, a novel electrochemical sensor based on graphitic carbon nitride nanosheets decorated bovine serum albumin@$MnO_2$ (g-$C_3N_4$NS/BSA@$MnO_2$) nanocomposite and molecularly imprinted polymers (MIPs) was developed and applied to rice samples for ZEA determination. Firstly, the synthesis of bulk g-$C_3N_4$ by thermal poly-condensation method was completed. After the ultra-sonication treatment of bulk g-$C_3N_4$ providing graphitic carbon nitride nanosheets, the nanocomposite was successfully produced via electrostatic forces between g-$C_3N_4$NS and BSA@$MnO_2$. Then, a novel MIP-based electrochemical electrode including g-$C_3N_4$NS/BSA@$MnO_2$ was prepared in the presence of ZEA as target analyte and pyrrole (Py) monomer by cyclic voltammetry (CV). The formed electrochemical sensor exhibited a linearity of 1.0 – 10.0 ng $L^{-1}$ with a detection limit (LOD) of 0.25 ng $L^{-1}$. Furthermore, the high selectivity, reproducibility and stability of the prepared MIPebased electrochemical sensor exhibited that it could be used in real sample analysis such as rice.

## 1. Introduction

Mycotoxins are secondary metabolites produced by *Aspergillus* and among the most common food pollutants (Wu et al., 2021). They are commonly found in agri-food products such as cereals and fruit juice and are associated with a variety of health outcomes including carcinogenic and hepatotoxic effects (Martins et al., 2020). Mycotoxin contamination is dependent on physicochemical parameters such as ambient temperature and pH value (Pleadin et al., 2019). ZEA has been frequently detected in different grains such as sesame, straw, flour, malt, soybean, beer, and corn oil. Because of its negative effects on human health, the maximum limits allowed for food products have been determined as 20.0 μg $kg^{-1}$ in child and baby foods, 50.0 μg $kg^{-1}$ in cereal and 200.0 μg $kg^{-1}$ in unprocessed corn (Rogowska et al., 2019). In addition, ZEA and its metabolites bind competitively to estrogen receptors and affect the synthesis and release of sex hormones (Martins et al., 2020). Although the main target of ZEA toxicity is the reproductive system, it has been reported that it also adversely affects the gastrointestinal tract (Abassi et al., 2016).

There are traditional analytical methods for ZEA analysis including HPLC, ELISA, capillary electrophoresis, surface plasmon resonance (SPR), solid phase extraction and MS (Çapar et al., 2023; Goud et al., 2018; Mahato et al., 2021). Generally, analysis with the combination of HPLC and MS is dominant in the literature. A reference method standardized and approved by the European Committee for Standardization for the determination of ZEA in corn-based infant formula and grain-based foods using immunoaffinity and fluorescence detection is also available. Although these methods have high specificity, they require qualified manpower to operate. In addition, despite their good accuracy, the complex preprocessing of samples, dependence on operator competence, and variability of test results do not guarantee fast determination of large numbers of samples (Guo et al., 2023). Electrochemical sensors do not require complex laboratory tools for mycotoxin detection in biological models (Bölükbasi et al., 2022). The sensitivity of electrochemical detection methods allows for cheap and rapid recognition (Yıldırım et al., 2023). Therefore, electrochemical methods will be a

* Corresponding author.
*E-mail address:* mlutfi.yola@hku.edu.tr (M.L. Yola).

https://doi.org/10.1016/j.jfca.2023.105857
Received 1 October 2023; Received in revised form 16 November 2023; Accepted 21 November 2023
Available online 23 November 2023

unique technique for the determination of mycotoxins such as ZEA. Electrochemical sensor techniques can be used directly for target molecules with possible oxidative and reducing groups. However, there are some disadvantages such as poor specificity and selectivity in the electrochemical sensor applications. Hence, various recognition elements such as MIPs and nanocomposites are used to develop highly sensitive and selective electrochemical sensors (Deveci et al., 2023). Especially, MIPs are capable of molecular recognition and their preparations can be controlled under difficult conditions such as strong acids, strong bases, organic solvents and high temperatures. The preparation of molecularly imprinted polymers consists of three steps including pre-complexation, polymerization and removal of the analyte molecule. After the removal process, three-dimensional nanocavities specific to the analyte molecule are formed, which enables the use of selective sensor designs (Rebelo et al., 2021; Wang et al., 2023). As a result, their high affinity and specificity for the target molecule have generated a growing interest in their use in sensors as an alternative recognition element to enzymes, antibodies, and natural receptors. In the literature, several MIP-based electrochemical sensors were developed and applied to ZEA detection. For example, a flower-like nanocomposite-modified electrode based on $Tb^{3+}/Co_3O_4$ was prepared for ZEA detection and a linearity of 0.001–500.0 μmol $L^{-1}$ and a LOD of 0.34 nmol $L^{-1}$ were obtained (Zaman et al., 2023). Secondly, a PEGylated $Fe_3O_4$ nanoparticles-based MIP electrochemical sensor was presented for ZEA detection in food samples. A linearity of 0.34–1.12 fg $mL^{-1}$ and recovery of 92.0–106.0% showed the formation of a sensitive and selective electrochemical sensor (Naidoo et al., 2023). Finally, AuNPs/reduced graphene nanoribbons including a MIP was constructed for ZEA determination in food samples and a linearity of 1.00 – 500.0 ng $mL^{-1}$ was obtained (Zhou et al., 2023). All these studies showed that MIP and nanocomposite-based sensor systems can be used especially for mycotoxin determinations.

Graphitic carbon nitride (g-$C_3N_4$) as a semiconductor material has started to receive intense interest because of its superior chemical/physical stability, catalytic features and electronic structure (Çapar et al., 2023; Ong et al., 2016). g-$C_3N_4$ material with tri-s-triazine units has been frequently used in sensor applications (Yola, 2022). The g-$C_3N_4$NS prepared by ultra-sonication of g-$C_3N_4$ has important applications due to its high quantum yield and bioimaging (Liao et al., 2020). g-$C_3N_4$NS can be efficiently integrated with other active nanomaterials because of its specific surface area in comparison with quantum dots and carbon dots (Zhang et al., 2013). For example, g-$C_3N_4$NS-decorated $MnO_2$ nanoparticles nanocomposite was synthesized and used as a fluorescence probe for glutathione analysis (Zhang et al., 2014b). In addition, its other composites including metal nanoclusters were developed and utilized for sensor applications (Guo et al., 2016).

$MnO_2$ nanomaterial exhibited significant features due to its facile synthesis and low toxicity (Wang et al., 2020). In addition, it demonstrated the fast electron transfer ability, strong oxidizing and absorption features (Wang et al., 2019a). In particular, $MnO_2$/g-$C_3N_4$ composites have important applications such as enzyme activity determination (Zhang et al., 2021). Nonetheless, the direct incorporation of $MnO_2$ into g-$C_3N_4$ can decrease the surface stability and biocompatibility owing to $MnO_2$'s hydrophobicity. To eliminate this problem, BSA was utilized as a template for improving the stability degree in this study.

This work contains an electrochemical sensor based on graphitic carbon nitride nanosheets-decorated bovine serum albumin@$MnO_2$ and molecularly imprinted polymer for ZEA determination in rice samples. After the synthesis of g-$C_3N_4$NS/BSA@$MnO_2$ nanocomposite with high purity and yield, the prepared molecularly imprinted sensor based on g-$C_3N_4$NS/BSA@$MnO_2$ nanocomposite was applied to ZEA analysis in flour samples. Thanks to the prepared sensor in this study, ZEA detection will be done quickly and with high precision. Thus, it will be a seminal work in detecting other mycotoxins more accurately and selectively. Moreover, thanks to this sensor, early diagnosis of the diseases caused by mycotoxin poisoning will be possible in future.

## 2. Experimental

### 2.1. Materials

ZEA, aflatoxin B1 (AFB1), fumonisin B1 (FB1), ochratoxin A (OTA), patulin (PAT), deoxynivalenol (DON), citrinin (CIT), bovine serum albumin (BSA), melamine (MEL), manganese acetate (MA, $MnAc_2.4\,H_2O$), sodium hydroxide (NaOH), sodium chloride (NaCl), ethyl alcohol (EtOH), acetonitrile (ACN) and Py monomer were purchased from Sigma-Aldrich. Phosphate-buffered saline (pH 6.0, PBS) (0.1 mol $L^{-1}$) was selected as a supporting electrolyte.

### 2.2. Instrumentation

The morphological analyses of scanning electron microscopy (SEM), transmission electron microscopy (TEM), x-ray diffraction analysis (XRD), Fourier-transform infrared spectroscopy (FTIR) and x-ray photoelectron spectroscopy (XPS) were carried out by using ZEISS EVO 50 SEM (Germany), JEOL 2100 TEM (Tokyo, Japan), Rikagu Miniflex x-ray diffractometer (Tokyo, Japan), Bruker-Tensor 27 FTIR spectrometer (Tokyo, Japan) and PHI 5000 Versa Probe type x-ray photoelectron spectrometer (Japan/USA), respectively. The square wave voltammetry (SWV), electrochemical impedance spectroscopy (EIS), and cyclic voltammetry (CV) measurements were performed by using a Gamry Reference 600 workstation (USA).

### 2.3. Preparation of g-$C_3N_4$NS and g-$C_3N_4$NS/BSA@$MnO_2$ nanocomposite

The synthesis of bulk g-$C_3N_4$ was completed by the thermal polycondensation method (Yola et al., 2016). In this technique, after the transfer of MEL (10.00 g) in an alumina crucible, the heating treatment was performed at 630 °C with a rising rate of 5 °C $min^{-1}$ for 1 h. After cooling at 25 °C, the yellow bulk g-$C_3N_4$ was stored at 25 °C and pulverized in a mortar. Afterwards, bulk g-$C_3N_4$ was ultra-sonicated in 50.0 mL distilled water for 10 h to obtain ultra-thin g-$C_3N_4$ (**g-$C_3N_4$NS**) and dried at 20 °C.

For the synthesis of BSA@$MnO_2$ nanoparticles, MA (50.0 mmol $L^{-1}$, 150.00 μL) was transported into BSA solution (10.00 mg $mL^{-1}$, 5.00 mL) under strong mixing for 5 min. Then, NaOH (1.0 mol $L^{-1}$, 5.00 mL) was slowly added into above solution for 6 h. The adjustment of pH was controlled in 10–11. The brown solution confirmed the presence of **BSA@$MnO_2$** and it was purified in distilled water. g-$C_3N_4$NS/BSA@$MnO_2$ nanocomposite was prepared via electrostatic forces between g-$C_3N_4$NS and BSA@$MnO_2$. BSA@$MnO_2$ (15.00 mg $mL^{-1}$, 4.00 mL) was slowly added into g-$C_3N_4$NS (0.20 mg $mL^{-1}$, 2.00 mL) for 10 h. The prepared **g-$C_3N_4$NS/BSA@$MnO_2$** nanocomposite was stored at 20 °C (Sun et al., 2023).

### 2.4. Production of g-$C_3N_4$NS/BSA@$MnO_2$ modified glassy carbon electrode (g-$C_3N_4$NS/BSA@$MnO_2$ /GCE)

The cleaning procedure of GCE was explained in detail in our previous study (Yola et al., 2012). After cleaning treatment, g-$C_3N_4$NS/BSA@$MnO_2$ solution (10.0 μL, 0.10 mg $mL^{-1}$) was dropped on the GCE surface and dried at 25 °C, providing **g-$C_3N_4$NS/BSA@$MnO_2$/GCE**. **g-$C_3N_4$NS/GCE** and **BSA@$MnO_2$/GCE** surfaces were developed via the procedure above. The prepared modified electrode surfaces including strong physical interactions between GCE and nanomaterials were stored in a small closed cabinet at 25 °C without temperature and pressure changes.

### 2.5. Development of ZEA imprinted sensor and ZEA removal

Preparation of ZEA imprinted g-$C_3N_4$NS/BSA@$MnO_2$/GCE (**MIP/g-$C_3N_4$NS/BSA@$MnO_2$/GCE**) was carried out in 100.0 mmol $L^{-1}$ Py in

0.1 M PBS (pH 6.0) including 25.0 mmol $L^{-1}$ ZEA. Py was used as a monomer in this study owing to its high conductivity, electropolymerization efficiency and high physical inertness (Deveci et al., 2023). As a result of the potential scanning performed in the range of + 0.0/+ 1.0 V, it was seen that the polymerization peaks appearing at approximately + 0.700 V decreased as the number of scans increased. After these 20 scans were completed, the prepared MIP electrodes were stored at room temperature. Scheme 1 exhibited the preparation of g-$C_3N_4$NS/BSA@$MnO_2$ nanocomposite and ZEA imprinted electrode. ZEA non-imprinted g-$C_3N_4$NS/BSA@$MnO_2$/GCE (**NIP/g-$C_3N_4$NS/BSA@$MnO_2$/GCE**) was improved by the above procedure without ZEA to exhibit the imprinting selectivity.

For ZEA removal from the electrode surface, all MIP and NIP electrodes prepared for desorption studies were placed in 25.0 mL flasks containing 0.1 mol $L^{-1}$ NaCl. Afterwards, these flasks were kept at room temperature during the desorption time for 20 min at low agitation speed and these electrodes were kept in a closed place so that they would not be affected by pressure and temperature changes by drying the nitrogen gas.

### 2.6. Sample preparation

After the rice samples purchased (0.20 g) in Gaziantep were pulverized, they were transferred into EtOH:ACN mixture (20.00 mL, 1:1, v/v) under strong mixing for 20 min. The centrifugation (20 min at 10000 rpm) was applied to the samples. After 20 min, the upper phase was diluted with 0.1 mol $L^{-1}$ PBS (20.00 mL, pH 6.0) for electrochemical measurements. SWV, a fast voltammetric technique, was used for electrochemical analysis. Firstly, pH 6.0 PBS was added to the electrochemical cell. After increasing concentrations of ZEA standard solutions (from 1.0 ng $L^{-1}$ to 10.0 ng $L^{-1}$) were added to the pH 6.0 PBS, the potential application from + 0.6 V to + 1.4 V was performed by using SWV. ZEA determination was performed from real samples from the calibration equation obtained by plotting the peak currents occurring at + 1.0 V against standard ZEA concentrations.

## 3. Results and discussion

### 3.1. Characterizations of g-$C_3N_4$NS/BSA@$MnO_2$ nanocomposite

g-$C_3N_4$NS was obtained by the liquid exfoliation and acidification of bulk graphitic carbon nitride, which was obtained by the thermal polymerization of melamine (Zhang et al., 2015a). The small size of g-$C_3N_4$NS was shown in Fig. 1 A. Fig. 1B showed the BSA@$MnO_2$ structure with a particle diameter of several nanometers and the nanostructure of g-$C_3N_4$NS/BSA@$MnO_2$ including a clear layer with black dots was given on Fig. 1 C. In addition, the HRTEM image (Fig. 2 A) of g-$C_3N_4$NS showed a lattice space of 0.332 nm, which corresponded to the (002) lattice plane of bulk graphitic carbon nitride (Ma et al., 2015). According to Fig. 2B, a lattice space of 0.361 nm attributing to g-$C_3N_4$NS/BSA@$MnO_2$ nanocomposite was in harmony with the (220) lattice plane of α-$MnO_2$ (Tan et al., 2017). Finally, the average size distributions of g-$C_3N_4$NS, BSA@$MnO_2$ and g-$C_3N_4$NS/BSA@$MnO_2$ nanocomposite were obtained as 79.240 ± 0.011 nm, 3.190 ± 0.022 nm and 88.390 ± 0.007 nm by dynamic light scattering measurements, respectively (Fig. S1). The average size of g-$C_3N_4$NS/BSA@$MnO_2$ nanocomposite was larger in comparison with its g-$C_3N_4$NS, providing BSA@$MnO_2$'s successful adsorption on g-$C_3N_4$NS.

Fig. S2 exhibited UV-Vis absorption and fluorescence spectra of g-$C_3N_4$ NS. Red spectra including the absorption band showed an evident absorption peak at about 296 nm (Sun et al., 2023) and the blue spectra including the emission band exhibited an evident emission peak at about 459 nm under an excitation of 350 nm. Moreover, UV-Vis absorption spectra of BSA, BSA@$MnO_2$ and g-$C_3N_4$NS/BSA@$MnO_2$ nanocomposite were obtained (Fig. S3A). The evident absorption band of BSA was obtained at 280 nm and a different absorption band in the range of 300–500 nm was observed for BSA@$MnO_2$, indicating the successful formation of $MnO_2$ NPs (Yu et al., 2019). When we investigate the absorption spectrum of g-$C_3N_4$NS/BSA@$MnO_2$ nanocomposite, the absorption bands at about 296 nm and 280 nm confirmed the successful preparation of g-$C_3N_4$NS/BSA@$MnO_2$ nanocomposite. Zeta potentials (Fig. S3B) of g-$C_3N_4$NS, g-$C_3N_4$NS acidification, BSA@$MnO_2$ and

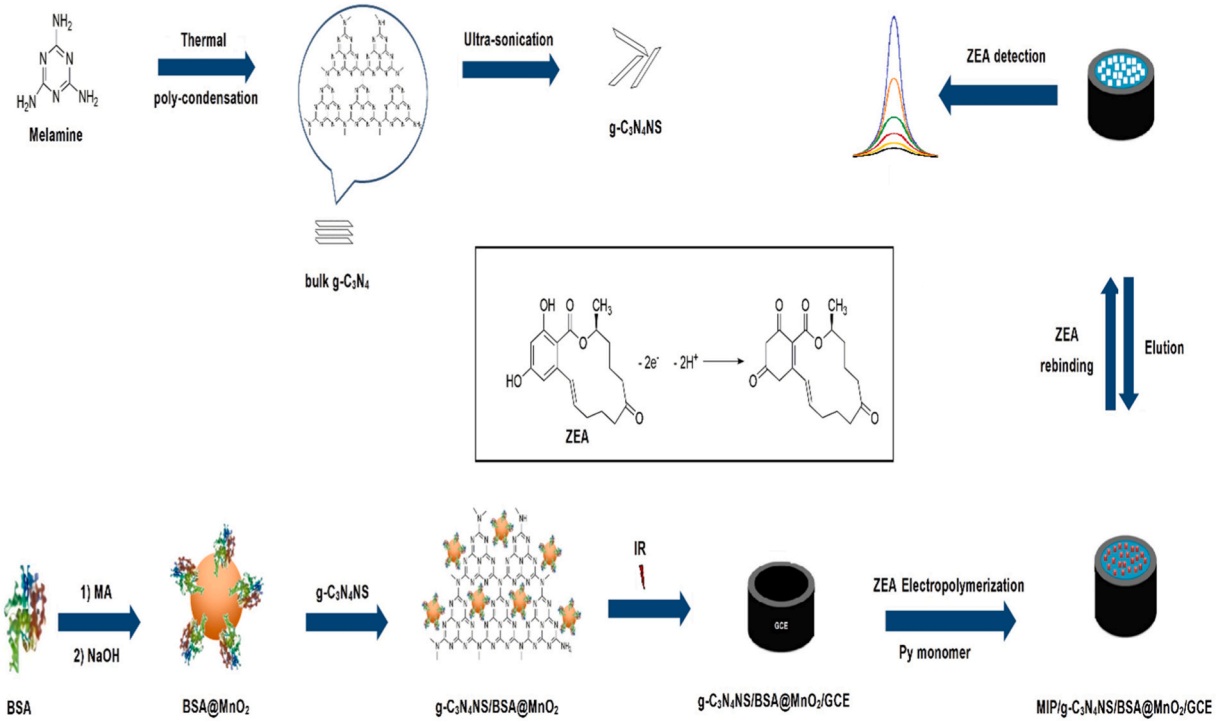


**Scheme 1.** Preparation of g-$C_3N_4$NS/BSA@$MnO_2$ nanocomposite and ZEA imprinted electrode.

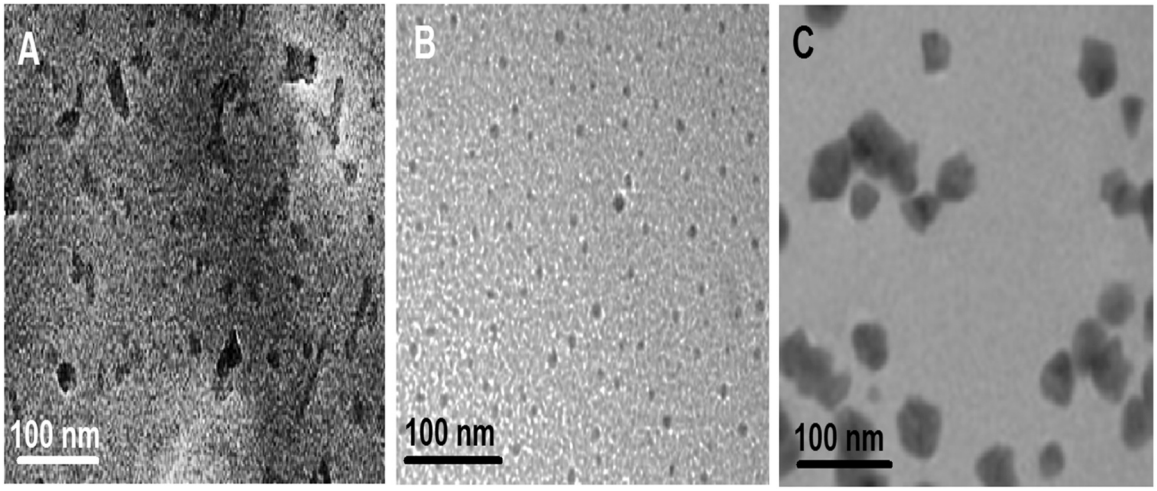


**Fig. 1.** (A) TEM images of (A) g-$C_3N_4$NS, (B) BSA@$MnO_2$ and (C) g-$C_3N_4$NS/BSA@$MnO_2$ nanocomposite.

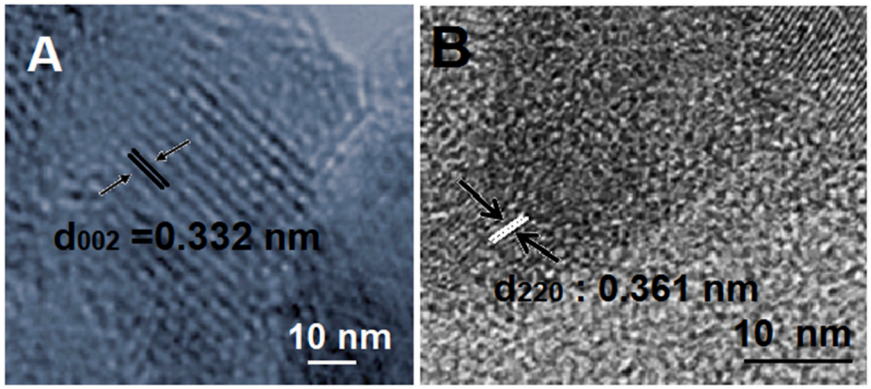


**Fig. 2.** (A) HRTEM images of (A) g-$C_3N_4$NS and (B) g-$C_3N_4$NS/BSA@$MnO_2$ nanocomposite.

g-$C_3N_4$NS/BSA@$MnO_2$ nanocomposite were calculated. Electrostatic interactions between g-$C_3N_4$NS and BSA@$MnO_2$ provided the construction of nanocomposite. Surface potential value of − 22.890 ± 0.037 mV belonging to g-$C_3N_4$NS changed to + 20.070 ± 0.043 mV owing to protonation process in $HNO_3$ solution (Kumar et al., 2020). In addition, the surface potential value of − 29.870 ± 0.067 mV belonging to BSA@$MnO_2$ indicated the presence of Mn–O groups of $MnO_2$ NPs, confirming the successful adsorption of BSA@$MnO_2$ on g-$C_3N_4$NS via electrostatic interactions (Wang et al., 2019a).

XRD patterns of bulk g-$C_3N_4$, g-$C_3N_4$NS and g-$C_3N_4$NS/BSA@$MnO_2$ nanocomposite were given in Fig. S4A. Two XRD peaks corresponding to bulk g-$C_3N_4$ at 14.07° and 28.03° were attributed to (100) tri-s-triazine units and (002) π-π conjugated aromatic groups, respectively (Wu et al., 2020). After the formation of g-$C_3N_4$NS, the intensities of these two XRD peaks at 14.07° and 28.03° slightly decreased (Sun et al., 2023; Ti et al., 2021). On XRD pattern of g-$C_3N_4$NS/BSA@$MnO_2$ nanocomposite, 26.67°, 29.07° and 40.08° corresponding to (220), (310), and (211) confirmed the formation of tetragonal α-$MnO_2$ phase. According to FTIR spectra (Fig. S4B) of bulk g-$C_3N_4$, g-$C_3N_4$NS and g-$C_3N_4$NS/BSA@$MnO_2$ nanocomposite, bulk g-$C_3N_4$ and g-$C_3N_4$NS exhibited sharp peaks at about 810 $cm^{-1}$ attributing to tri-s-triazine vibrations. In addition, the absorption bands between 1235 $cm^{-1}$ and 1610 $cm^{-1}$ corresponded to aromatic C–N groups' stretching and the peak at 3183 $cm^{-1}$ corresponded to the amine groups' stretching (Wu et al., 2020). The absorption bands at about 3215 $cm^{-1}$ and 1648 $cm^{-1}$ on the FTIR spectrum of g-$C_3N_4$NS were attributed to –OH and –C═O groups, respectively (Ti et al., 2021). Finally, the absorption band at about 555 $cm^{-1}$ corresponded to Mn–O groups' vibration modes on the FTIR spectrum of g-$C_3N_4$NS/BSA@$MnO_2$ nanocomposite (Li et al., 2021).

XPS spectra of g-$C_3N_4$NS/BSA@$MnO_2$ nanocomposite were obtained to determine the elemental constitution (Fig. 3). Two XRD peaks at 652.83 and 641.93 eV on the Mn2p spectrum corresponded to Mn2p1/2 and Mn2p3/2, respectively (Wang et al., 2020). Four XPS peaks at 532.43, 531.89, 531.19, and 530.37 eV on the O1s spectrum corresponded to –C–O–H/H–O–H, Mn–O–H, –N–C═O and Mn–O–Mn, respectively (Wang et al., 2019b). For the N1s spectrum, three XPS peaks at 400.84, 399.17 and 397.83 eV attributed to –N–Hx, N–C/N–$(C)_3$ and –C═N–C–, respectively confirmed the presence of g-$C_3N_4$NS (Zhang et al., 2015b). Finally, four XPS peaks at 288.17, 287.49, 286.17 and 285.12 eV relating to –N–C═O/O–C═O, –C–N = C–, –C–N and –C–C–, respectively indicated the successful formation of nanocomposite (Wang et al., 2020).

### 3.2. *Electrochemical characterizations of g-$C_3N_4$NS, BSA@$MnO_2$ and g-$C_3N_4$NS/BSA@$MnO_2$ nanocomposite modified electrodes*

Electrochemical characterizations of the successfully synthesized nanomaterials such as g-$C_3N_4$NS, BSA@$MnO_2$ and g-$C_3N_4$NS/BSA@$MnO_2$ nanocomposite were performed using CV and EIS techniques. Firstly, the evident anodic and cathodic peaks were obtained on bare GCE in the presence of 5.0 mmol $L^{-1}$ $[Fe(CN)_6]^{3-/4-}$ containing 0.1 mol $L^{-1}$ KCl (curve a of Fig. S5A). When g-$C_3N_4$NS modified glassy carbon electrode (g-$C_3N_4$NS/GCE) was utilized, anodic and cathodic peak currents were improved (curve b of Fig. S5A) owing to g-$C_3N_4$NS' graphite-like structure having strong covalent bonds between carbon and nitride atoms providing the increased electrical feature (Zhang

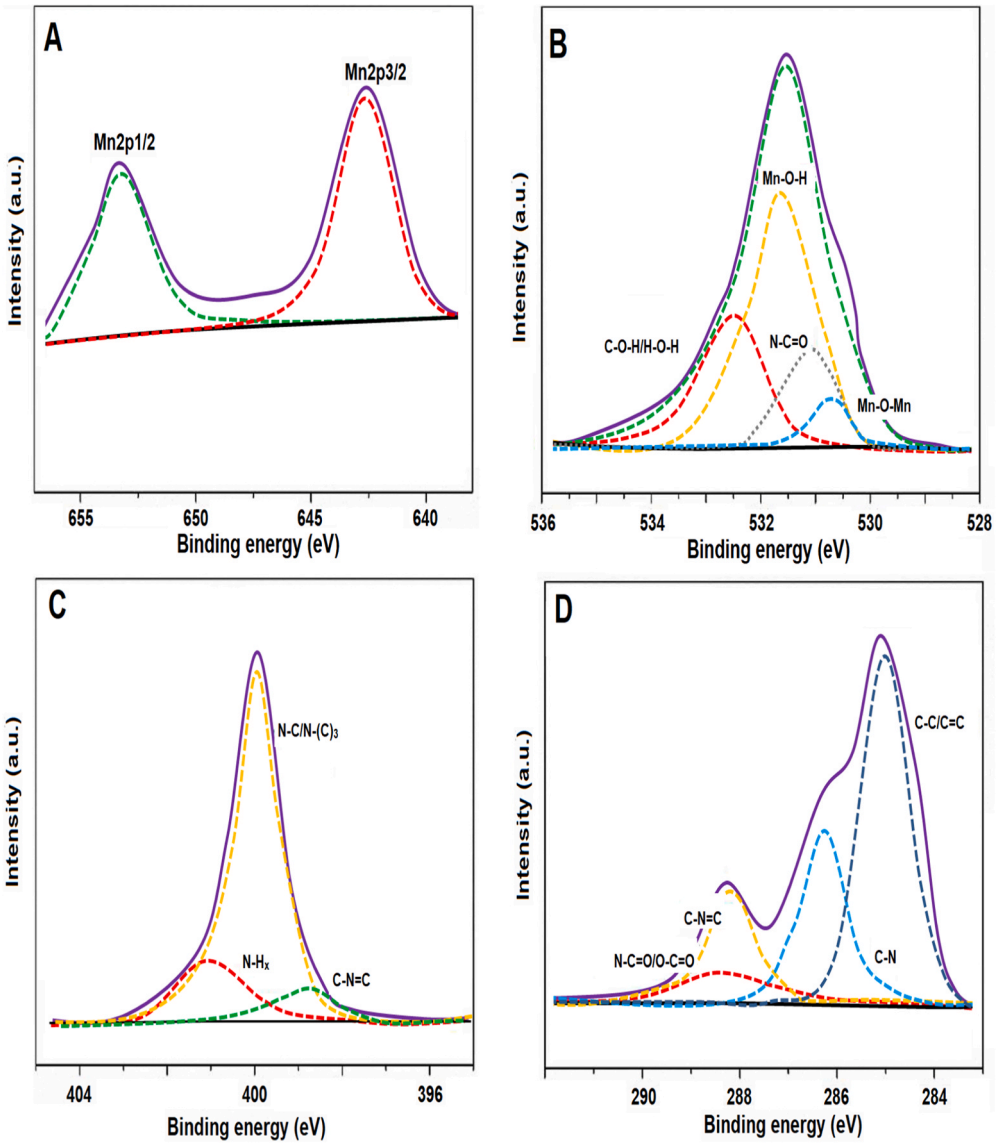


**Fig. 3.** XPS spectra (A) Mn2p, (B) O1s (C) N1s and (D) C1s spectra of g-$C_3N_4$NS/BSA@$MnO_2$ nanocomposite.

et al., 2014a). An evident increase in anodic and cathodic peaks occurred on BSA@$MnO_2$/GCE (curve c of Fig. S5A) due to $MnO_2$ nanoparticles' fast electron transfer ability (Sun et al., 2023; Wang et al., 2019a). Lastly, because of $MnO_2$ nanoparticles' quench ability into g-$C_3N_4$NS improving electrochemical sensor activity, the highest anodic and cathodic peak currents were obtained by using g-$C_3N_4$NS/BSA@$MnO_2$/GCE (curve d of Fig. S5A) (Zhang et al., 2014b). Furthermore, the electrochemically active electrode areas were calculated in presence of 1.0 mmol $L^{-1}$ $[Fe(CN)_6]^{3-}$ by using the equation of $i_p = 2.69 \times 10^5$ A $n^{3/2}$ $D^{1/2}$ C $v^{1/2}$ and the surface areas of bare GCE, g-$C_3N_4$NS/GCE, BSA@$MnO_2$/GCE, and g-$C_3N_4$NS/BSA@$MnO_2$/GCE were obtained as $0.072 \pm 0.007$ $cm^2$, $0.473 \pm 0.003$ $cm^2$, $0.617 \pm 0.002$ $cm^2$ and $0.894 \pm 0.006$ $cm^2$, respectively. The results of the obtained electrochemically active electrode area showed that the synergistic effect between g-$C_3N_4$NS and BSA@$MnO_2$ has a performance-enhancing effect for sensor applications in real samples.

EIS measurements (Fig. S5B) were also recorded and the charge transfer resistance ($R_{ct}$) values were obtained to be $91.000 \pm 0.008$ ohm for bare GCE (curve a), $75.000 \pm 0.001$ ohm for g-$C_3N_4$NS/GCE (curve b), $65.000 \pm 0.004$ ohm for BSA@$MnO_2$/GCE (curve c), and $55.000 \pm 0.003$ ohm for g-$C_3N_4$NS/BSA@$MnO_2$/GCE (curve d). According to the EIS results, it was seen that the electrochemical sensor activity was higher on g-$C_3N_4$NS/BSA@$MnO_2$/GCE with the lowest $R_{ct}$ value, and these results agreed with CV values.

### 3.3. Development of ZEA imprinted polymer on g-$C_3N_4$NS/BSA@$MnO_2$/GCE

ZEA imprinted polymer on g-$C_3N_4$NS/BSA@$MnO_2$/GCE was developed in the presence of 25.0 mmol $L^{-1}$ ZEA as the target molecule including 100.0 mmol $L^{-1}$ Py as the monomer. Oxidation peak currents belonging to ZEA including Py on g-$C_3N_4$NS/BSA@$MnO_2$/GCE, which appeared at approximately + 0.700 V in the first scan, decreased as the number of scans increased. Hence, this current decreases on the working electrode provided the emergence of ZEA imprinted polymer on g-$C_3N_4$NS/BSA@$MnO_2$/GCE (Fig. S6A).

To demonstrate the high affinity gained in molecularly imprinted technology, NIP electrodes (NIP/g-$C_3N_4$NS/BSA@$MnO_2$/GCE) were prepared without the target molecule (ZEA) under the same conditions and square wave voltammograms (SWVs) were recorded by MIP and NIP electrodes in the presence of 10.0 ng $L^{-1}$ ZEA (Fig. S6B). According to curve a of Fig. S6B, no electrochemical signals were observed on the MIP electrode without the ZEA molecule as expected. The affinity gained against the ZEA molecule using the MIP electrode (curve c of Fig. S6B)

was approximately 10 times the affinity obtained using the NIP electrode (curve b of Fig. S6B) in the presence of 10.0 ng $L^{-1}$ ZEA. Thus, these electrochemical results verified the gained superior selectivity by imprinting technique. MIP electrodes (MIP/g-$C_3N_4$NS/GCE, MIP/BSA@$MnO_2$/GCE, MIP/g-$C_3N_4$NS/BSA@$MnO_2$/GCE) of each of the materials prepared step by step were designed and SWVs were recorded using each MIP electrodes in presence of 10.0 ng $L^{-1}$ ZEA (Fig. S6C). Hence, obtaining the highest current signal using the MIP/g-$C_3N_4$NS/BSA@$MnO_2$/GCE electrode confirmed the CV results in Section 3.2. Finally, SEM analyses were performed to see the morphological differences between MIP/g-$C_3N_4$NS/BSA@$MnO_2$/GCE and NIP/g-$C_3N_4$NS/BSA@$MnO_2$/GCE electrodes. According to Fig. S7, it is understood that polymeric nanocavities were seen in the MIP electrode but not in the NIP electrode.

The study of the electrochemical mechanism of ZEA on the MIP/g-$C_3N_4$NS/BSA@$MnO_2$/GCE surface was tried to be elucidated. The hydroxyl groups were oxidized to a benzoquinone structure in the oxidation mechanism including two electrons and two protons (Scheme 1) (Zeng et al., 2022).

### 3.4. Optimization

#### 3.4.1. pH effect

In MIP electrode applications, pH is the most influential factor in the electrochemical behavior of the electrode surface. According to Fig. S8A, electrochemical measurements of the developed MIP electrode in the pH 4.0–8.0 range were made in the presence of 10.0 ng $L^{-1}$ ZEA and the most optimum and highest electrochemical response was measured in the presence of pH 6.0 PBS. Moreover, the linear effect of pH on the oxidation potential was investigated and Ep(V) $= -0.0578$ pH$+ 1.137$ equation was found. The obtained slope value (0.0578) was close to the theoretical value (0.0590) and this result verified the equal number of protons and electrons in the electrochemical process (Scheme 1).

#### 3.4.2. Mole ratio ZEA to Py monomer effect

In MIP electrode preparation, since the formation of a thick monomer film on the electrode surface may cause undesired interactions between the monomer-analyte on the surface, significant issues affecting the accuracy and sensitivity of the developed sensor can arise. In the opposite case, the formation of a thin film layer can cause complex breakage from the electrode surface, which can create a significant disadvantage, especially in terms of repeatability. Thus, we observed that the highest electrochemical currents were measured when 100.0 mmol $L^{-1}$ Py and 25.0 mmol $L^{-1}$ ZEA were used (Fig. S8B).

#### 3.4.3. Desorption time effect

In this type of MIP sensor, the complete removal of the targeted analyte molecule from the electrode surface with a suitable desorption agent is important for the kinetics of the electrochemical reaction. In this study, desorption times of 10–50 min were applied to separately developed MIP-type electrodes and electrochemical signals remained stable after 20 min (Fig. S8C). Thus, the desorption time of 20 min was used for subsequent analytical applications.

#### 3.4.4. Scan cycle effect

CV scan number effect is important for the homogeneity of the MIP electrode surface, as is the molar ratio effect. According to Fig. S8D, four MIP electrodes with different scan numbers (10, 20, 30, 40 and 50) were prepared and each was used in the presence of 10.0 ng $L^{-1}$ ZEA. The highest current signals were seen with the 20th scan cycle.

### 3.5. Sensitivity of the developed MIP electrode

The calibration equation as y (μA) $= 1.0765$x ($C_{ZEA}$, ng$L^{-1}$) - 0.0123, ($R^2 = 0.999$) was obtained by using the current values obtained by applying the MIP-based electrode developed to ZEA standard solutions at increasing concentrations (Fig. 4) and the values of quantification limit (LOQ) and LOD were calculated as 1.0 ng $L^{-1}$ (0.001 ng $mL^{-1}$), and 0.25 ng $L^{-1}$ (0.00025 ng $mL^{-1}$), respectively (See Supplementary Data for the equations). Furthermore, Table 1 demonstrated a comparison of MIP/g-$C_3N_4$NS/BSA@$MnO_2$/GCE with the other reported methods in terms of sensitivity. According to the obtained comparative results, it can be said that the developed sensor has a high sensitivity for ZEA analysis. In addition, we can say that a sensor system suitable for Green Chemistry can be easily presented since the formation of composite material is carried out with a chemical technique with the least waste generation during the sensor preparation. According to the incubation/elution times of the published works, thanks to the developed sensor, ZEA determination took place in a shorter time. As a result, thanks to this MIP-based sensor, which is easily prepared in laboratory conditions, the analysis of mycotoxins can be done quickly and sensitively and early diagnosis of health problems, which may arise from pesticide poisoning, can be made with a high selectivity. In addition, the problem of access to safe foods and foods, which is a global problem all over the world, can be minimized by designing such sensors.

### 3.6. Recovery studies

In order to demonstrate the utility of the developed sensor in real samples with high selectivity, standard ZEA solutions with increasing concentrations were added to the divided rice samples into 4 equal small tubes, except the first test tube (Table S1). According to the values of recovery studies, the recovery results close to 100.00% show that the developed sensor has a high selectivity. Moreover, it appears that other agents contained in the rice samples did not have any negative effect on the accuracy of the experimental results.

### 3.7. Selectivity, stability, and reproducibility of MIP/g-$C_3N_4$NS/BSA@$MnO_2$/GCE

During the ZEA analysis of the prepared MIP-based electrochemical sensor, selectivity tests were performed to prove its high selectivity in the presence of agents (CIT, PAT, AFB1, FB1, DON and OTA) with possible interference effects. For this, the obtained current signals by interacting both the MIP-based electrode (Fig. S9A) and the NIP-based electrode (Fig. S9B) with other agents 100 times higher than the ZEA concentration were recorded. The selectivity coefficient (k) and relative selectivity coefficient (k′) values were calculated using these current values (Table S2). MIP/g-$C_3N_4$NS/BSA@$MnO_2$/GCE was 15.385,

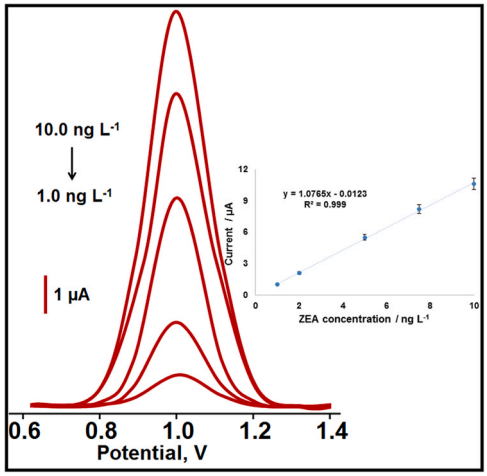


**Fig. 4.** (A) Effect of ZEA concentration on MIP/g-$C_3N_4$NS/BSA@$MnO_2$/GCE. Inset: Calibration curve of ZEA concentrations at MIP/g-$C_3N_4$NS/BSA@$MnO_2$/GCE in presence of pH 6.0 of PBS (from 1.0 ng $L^{-1}$ to 10.0 ng $L^{-1}$ ZEA).

**Table 1**
MIP/g-$C_3N_4$NS/BSA@$MnO_2$/GCE comparison with the reported other methods in terms of sensitivity.

| Material | Linear Range (ng $mL^{-1}$) | LOD (ng $mL^{-1}$) | Incubation/ Elution time | Ref. |
|---|---|---|---|---|
| MIP/AuNPs/rGO | 1.0 – 500.0 | 0.34 | 45 min | (Zhou et al., 2023) |
| CS-CNT-Pd | 0.25 – 16.0 | 0.25 | 3 h | (Kumar et al., 2023) |
| Ce-Ag/ZnO | 0.0 – 63.67 × $10^3$ | 260.00 | - | (Manjula et al., 2023) |
| S-g-$C_3N_4$/$Bi_2S_3$ | 0.001 – 0.01 | 0.00033 | 60 min | (Çapar et al., 2023) |
| Polyvalent aptamer | 0.01 – 2.0 | 0.0087 | 40 min | (He et al., 2024) |
| Multicolor immunosensor | 0.02 – 0.80 | 0.011 | 20 min | (Zhang et al., 2023) |
| **MIP/g-$C_3N_4$NS/ BSA@$MnO_2$/ GCE** | **0.001 – 0.01** | **0.00025** | **20 min** | **This study** |

16.667, 18.182, 25.000, 28.571 and 100.000 times more selective for ZEA than CIT, PAT, AFB1, FB1, DON and OTA, respectively, because of specific nano-cavities belonging to ZEA in the polymeric network located on the electrode surface. According to k′ values, it showed that MIP technology provided a high selectivity in target molecule analysis.

For the stability property of MIP/g-$C_3N_4$NS/BSA@$MnO_2$/GCE, the obtained current values of only one prepared MIP-based electrochemical sensor for 7 weeks were recorded (Fig. S10). The obtained current values at the end of the seventh week were approximately 98.391% of the obtained current values at the end of the first week, indicating a high stability of the prepared MIP-based sensor.

For the reproducibility property of MIP/g-$C_3N_4$NS/BSA@$MnO_2$/GCE, 25 MIP-based electrochemical electrodes were prepared individually according to the protocol described in Sections 2.3–2.5. The current values were recorded by using these 25 electrodes against 10.0 ng $L^{-1}$ ZEA analyte solution. The relative standard deviation of these 25 current values was 0.133%, indicating a high reproducibility.

## 4. Conclusions

We determined ZEA in rice samples by using a graphitic carbon nitride nanosheets decorated bovine serum albumin@$MnO_2$ nanocomposite-modified electrode including MIPs. Remarkable features of the developed molecularly imprinted electrochemical sensor such as electrode area and conductivity enhanced the sensor performances with a linearity of 1.0 – 10.0 ng $L^{-1}$. Using MIP/g-$C_3N_4$NS/BSA@$MnO_2$ as a sensor probe increased the loading of target molecules for signal amplification effect. In addition, since graphitic carbon nitride nanosheets decorated bovine serum albumin@$MnO_2$ nanocomposite with zero waste generation was produced, the developed sensor was suitable for Green Chemistry. In conclusion, the sensor exhibited a low LOD with 0.25 ng $L^{-1}$, superior selectivity, long-term stability, and high reproducibility. The obtained 100% recovery results proved that ZEA analysis could be performed with high accuracy. Thus, mycotoxin determination can be made more quickly, reliably and accurately by using this novel molecularly imprinted electrochemical sensor.

## CRediT authorship contribution statement

**Nesrin Çapar Rehman:** Conceptualization, Methodology, Writing - review & editing. **Neslihan Özdemir:** Data curation, Visualization, Investigation. **Havva Boyacıoğlu**: Writing - original draft, Visualization, Investigation. **Mehmet Lütfi Yola**: Supervision, Conceptualization, Writing - review & editing.

## Declaration of Competing Interest

The author declares that they have no known competing financial interests or personal relationships that could have appeared to influence the work reported in this paper.

## Data Availability

Data will be made available on request.

## Appendix A. Supporting information

Supplementary data associated with this article can be found in the online version at doi:10.1016/j.jfca.2023.105857.

## References


Abassi, H., Ayed-Boussema, I., Shirley, S., Abid, S., Bacha, H., Micheau, O., 2016. The mycotoxin zearalenone enhances cell proliferation, colony formation and promotes cell migration in the human colon carcinoma cell line HCT116. Toxicol. Lett. 254, 1–7.

Bölükbasi Ö, S., Yola, B.B., Karaman, C., Atar, N., Yola, M.L., 2022. Electrochemical α-fetoprotein immunosensor based on $Fe_3O_4$NPs@covalent organic framework decorated gold nanoparticles and magnetic nanoparticles including $SiO_2$@$TiO_2$. Microchim. Acta 189 (6), 242.

Çapar, N., Yola, B.B., Polat, İ., Bekerecioğlu, S., Atar, N., Yola, M.L., 2023. A zearalenone detection based on molecularly imprinted surface plasmon resonance sensor including sulfur-doped g-$C_3N_4$/$Bi_2S_3$ nanocomposite. Microchem. J. 193, 109141.

Deveci, H.A., Mavioğlu Kaya, M., Kaya, İ., Bankoğlu Yola, B., Atar, N., Yola, M.L., 2023. Bisphenol A imprinted electrochemical sensor based on graphene quantum dots with boron functionalized g-$C_3N_4$ in food samples. Biosensors 13 (7), 725.

Goud, K.Y., Kailasa, S.K., Kumar, V., Tsang, Y.F., Lee, S.E., Gobi, K.V., Kim, K.-H., 2018. Progress on nanostructured electrochemical sensors and their recognition elements for detection of mycotoxins: a review. Biosens. Bioelectron. 121, 205–222.

Guo, X., Wu, F., Ni, Y., Kokot, S., 2016. Synthesizing a nano-composite of BSA-capped Au nanoclusters/graphitic carbon nitride nanosheets as a new fluorescent probe for dopamine detection. Anal. Chim. Acta 942, 112–120.

Guo, Z., Gao, L., Yin, L., Arslan, M., El-Seedi, H.R., Zou, X., 2023. Novel mesoporous silica surface loaded gold nanocomposites SERS aptasensor for sensitive detection of zearalenone. Food Chem. 403, 134384.

He, Z., Zhang, J., Liu, M., Meng, Y., 2024. Polyvalent aptamer scaffold coordinating light-responsive oxidase-like nanozyme for sensitive detection of zearalenone. Food Chem. 431, 136908.

Kumar, A., Singh, S., Khanuja, M., 2020. A comparative photocatalytic study of pure and acid-etched template free graphitic $C_3N_4$ on different dyes: an investigation on the influence of surface modifications. Mater. Chem. Phys. 243, 122402.

Kumar, V.S., Kummari, S., Catanante, G., Gobi, K.V., Marty, J.L., Goud, K.Y., 2023. A label-free impedimetric immunosensor for zearalenone based on CS-CNT-Pd nanocomposite modified screen-printed disposable electrodes. Sens. Actuators B Chem. 377, 133077.

Li, B., Wang, X., Hong, S., Wang, Q., Li, L., Eltayeb, O., Dong, C., Shuang, S., 2021. $MnO_2$ nanosheets anchored with polypyrrole nanoparticles as a multifunctional platform for combined photothermal/photodynamic therapy of tumors. Food Funct. 12 (14), 6334–6347.

Liao, G., He, F., Li, Q., Zhong, L., Zhao, R., Che, H., Gao, H., Fang, B., 2020. Emerging graphitic carbon nitride-based materials for biomedical applications. Prog. Mater. Sci. 112, 100666.

Ma, Y., Liu, E., Hu, X., Tang, C., Wan, J., Li, J., Fan, J., 2015. A simple process to prepare few-layer g-$C_3N_4$ nanosheets with enhanced photocatalytic activities. Appl. Surf. Sci. 358, 246–251.

Mahato, D.K., Devi, S., Pandhi, S., Sharma, B., Maurya, K.K., Mishra, S., Dhawan, K., Selvakumar, R., Kamle, M., Mishra, A.K., Kumar, P., 2021. Occurrence, impact on agriculture, human health, and management strategies of zearalenone in food and feed: a review. Toxins 13 (2), 92.

Manjula, N., Pulikkutty, S., Chen, S.-M., 2023. 3D flower-like ceria silver co-doped zinc oxide catalyst assembled by nanorod for electrochemical sensing of zearalenone in food samples. Food Chem. 416, 135777.

Martins, C., Torres, D., Lopes, C., Correia, D., Goios, A., Assunção, R., Alvito, P., Vidal, A., De Boevre, M., De Saeger, S., Nunes, C., 2020. Food consumption data as a tool to estimate exposure to mycoestrogens. Toxins 12 (2), 118.

Naidoo, L., Uwaya, G.E., Meier, F., Bisetty, K., 2023. A novel electrochemical sensor for the detection of zearalenone in food matrices using PEGylated $Fe_3O_4$ nanoparticles supported by in-silico and multidetector AF4. J. Electroanal. Chem. 935, 117363.

Ong, W.-J., Tan, L.-L., Ng, Y.H., Yong, S.-T., Chai, S.-P., 2016. Graphitic carbon nitride (g-C3N4)-based photocatalysts for artificial photosynthesis and environmental remediation: are we a step closer to achieving sustainability? Chem. Rev. 116 (12), 7159–7329.

Pleadin, J., Frece, J., Markov, K., 2019. Chapter Eight - Mycotoxins in food and feed. In: Toldrá, F. (Ed.), Advances in Food and Nutrition Research. Academic Press, pp. 297–345.

Rebelo, P., Costa-Rama, E., Seguro, I., Pacheco, J.G., Nouws, H.P.A., Cordeiro, M.N.D.S., Delerue-Matos, C., 2021. Molecularly imprinted polymer-based electrochemical sensors for environmental analysis. Biosens. Bioelectron. 172, 112719.

Rogowska, A., Pomastowski, P., Sagandykova, G., Buszewski, B., 2019. Zearalenone and its metabolites: effect on human health, metabolism and neutralisation methods. Toxicon 162, 46–56.

Sun, X., Lei, P., Zhang, X., Wang, Q., Li, B., Shuang, S., Dong, C., 2023. The g-$C_3N_4$/BSA@$MnO_2$ nanocomposites fluorescent off-on probe for detection and imaging of ascorbic acid in living cells. Mater. Today Chem. 33, 101656.

Tan, X., Wan, Y., Huang, Y., He, C., Zhang, Z., He, Z., Hu, L., Zeng, J., Shu, D., 2017. Three-dimensional $MnO_2$ porous hollow microspheres for enhanced activity as ozonation catalysts in degradation of bisphenol A. J. Hazard. Mater. 321, 162–172.

Ti, M., Li, Y., Li, Z., Zhao, D., Wu, L., Yuan, L., He, Y., 2021. A ratiometric nanoprobe based on carboxylated graphitic carbon nitride nanosheets and Eu3+ for the detection of tetracyclines. Analyst 146 (3), 1065–1073.

Wang, L., Pagett, M., Zhang, W., 2023. Molecularly imprinted polymer (MIP) based electrochemical sensors and their recent advances in health applications. Sens. Actuators Rep. 5, 100153.

Wang, Q., Li, L., Wang, X., Dong, C., Shuang, S., 2020. Graphene quantum dots wrapped square-plate-like MnO2 nanocomposite as a fluorescent turn-on sensor for glutathione. Talanta 219, 121180.

Wang, Q., Wang, C., Wang, X., Zhang, Y., Wu, Y., Dong, C., Shuang, S., 2019a. Construction of CPs@$MnO_2$–AgNPs as a multifunctional nanosensor for glutathione sensing and cancer theranostics. Nanoscale 11 (40), 18845–18853.

Wang, Q., Zhang, Y., Wang, X., Wu, Y., Dong, C., Shuang, S., 2019b. Dual role of BSA for synthesis of $MnO_2$ nanoparticles and their mediated fluorescent turn-on probe for glutathione determination and cancer cell recognition. Analyst 144 (6), 1988–1994.

Wu, Y., Yang, D., Xu, W., Song, R., Li, M., Wang, Y., Zhou, B., Wu, N., Zhong, W., Cai, H.-l, Tu, J., Zhang, D., Wu, X.S., 2020. Tunable water-soluble carbon nitride by alkali-metal cations modification: enhanced ROS-evolving and adsorption band for photodynamic therapy. Appl. Catal. B 269, 118848.

Wu, Z., Pu, H., Sun, D.-W., 2021. Fingerprinting and tagging detection of mycotoxins in agri-food products by surface-enhanced Raman spectroscopy: Principles and recent applications. Trends Food Sci. Technol. 110, 393–404.

Yıldırım, M., Bölükbaşı, Ö.S., Parlak Özer, Z., Polat, İ., Atar, N., Yola, M.L., 2023. l-phenylalanine-imprinted electrochemical sensor based on $WS_2$ nanoflowers on N,B-doped graphene and its application to milk samples. Ind. Eng. Chem. Res. 62 (11), 4587–4594.

Yola, M.L., 2022. Carbendazim imprinted electrochemical sensor based on $CdMoO_4$/g-$C_3N_4$ nanocomposite: application to fruit juice samples. Chemosphere 301, 134766.

Yola, M.L., Atar, N., Qureshi, M.S., Üstündağ, Z., Solak, A.O., 2012. Electrochemically grafted etodolac film on glassy carbon for Pb(II) determination. Sens. Actuators B Chem. 171–172, 1207–1215.

Yola, M.L., Eren, T., Atar, N., 2016. A molecular imprinted voltammetric sensor based on carbon nitride nanotubes: application to determination of melamine. J. Electrochem. Soc. 163 (13), B588.

Yu, J., Yang, W., Xing, S., Wang, J., Han, H., Zhang, P., Xiang, C., Zhang, B., 2019. Blended gold/$MnO_2$@BSA nanoparticles for fluorometric and magnetic resonance determination of ascorbic acid. Microchim. Acta 186 (2), 89.

Zaman, G.S., Waleed, I., Obeid, R.A., Khudair, S.A., Al-Kahdum, S.A.A., Al-Majdi, K., Abed, A.S., Alsalamy, A., Qasim, M.T., Radie Alawadi, A.H., 2023. Electrochemical determination of zearalenone in agricultural food samples using a flower like nanocomposite-modified electrode. Mater. Chem. Phys. 305, 127986.

Zeng, Y., Camarada, M.B., Lu, X., Tang, K., Li, W., Qiu, D., Wen, Y., Wu, G., Luo, Q., Bai, L., 2022. Detection and electrocatalytic mechanism of zearalenone using nanohybrid sensor based on copper-based metal-organic framework/magnetic $Fe_3O_4$-graphene oxide modified electrode. Food Chem. 370, 131024.

Zhang, H., Huang, Q., Huang, Y., Li, F., Zhang, W., Wei, C., Chen, J., Dai, P., Huang, L., Huang, Z., Kang, L., Hu, S., Hao, A., 2014a. Graphitic carbon nitride nanosheets doped graphene oxide for electrochemical simultaneous determination of ascorbic acid, dopamine and uric acid. Electrochim. Acta 142, 125–131.

Zhang, J., Zhu, Z., Di, J., Long, Y., Li, W., Tu, Y., 2015a. A Sensitive Sensor for trace Hg2 + Determination Based on Ultrathin g-$C_3N_4$ Modified Glassy Carbon Electrode. Electrochim. Acta 186, 192–200.

Zhang, Q., Zhang, X., Zhang, G., Chen, W., Wu, S., Yang, H., Zhou, Y., 2023. Multicolor immunosensor for detection of zearalenone based on etching Au NBPs mediated by HRP. J. Food Compos. Anal. 115, 105014.

Zhang, X.-L., Zheng, C., Guo, S.-S., Li, J., Yang, H.-H., Chen, G., 2014b. Turn-on fluorescence sensor for intracellular imaging of glutathione using g-$C_3N_4$ nanosheet–$MnO_2$ sandwich nanocomposite. Anal. Chem. 86 (7), 3426–3434.

Zhang, X., Xie, X., Wang, H., Zhang, J., Pan, B., Xie, Y., 2013. Enhanced photoresponsive ultrathin graphitic-phase $C_3N_4$ nanosheets for bioimaging. J. Am. Chem. Soc. 135 (1), 18–21.

Zhang, Y., Wu, Y., Liu, L., Wang, W., Zhang, W., Song, D., Wang, X., Su, R., 2021. A dual-signal sensing platform based on nanosheet materials for ratiometric fluorescence and colorimetric detection of enzyme activities in human blood. Sens. Actuators B Chem. 346, 130531.

Zhang, Y., Zhang, Q., Shi, Q., Cai, Z., Yang, Z., 2015b. Acid-treated g-$C_3N_4$ with improved photocatalytic performance in the reduction of aqueous Cr(VI) under visible-light. Sep. Purif. Technol. 142, 251–257.

Zhou, B., Xie, H., Zhou, S., Sheng, X., Chen, L., Zhong, M., 2023. Construction of AuNPs/reduced graphene nanoribbons co-modified molecularly imprinted electrochemical sensor for the detection of zearalenone. Food Chem. 423, 136294.